

Local, global, and nonlinear screening in twisted double-layer graphene

Chih-Pin Lu^a, Martin Rodriguez-Vega^b, Guohong Li^a, Adina Luican-Mayer^{a,1}, Kenji Watanabe^c, Takashi Taniguchi^c, Enrico Rossi^b, and Eva Y. Andrei^{a,2}

^aDepartment of Physics and Astronomy, Rutgers, The State University of New Jersey, Piscataway, NJ 08855; ^bDepartment of Physics, College of William and Mary, Williamsburg, VA 23187; and ^cAdvanced Materials Laboratory, National Institute for Materials Science, 1-1 Namiki, Tsukuba 305-0044, Japan

Contributed by Eva Y. Andrei, May 4, 2016 (sent for review March 11, 2016; reviewed by Jeanie Lau and Allan H. MacDonald)

One-atom-thick crystalline layers and their vertical heterostructures carry the promise of designer electronic materials that are unattainable by standard growth techniques. To realize their potential it is necessary to isolate them from environmental disturbances, in particular those introduced by the substrate. However, finding and characterizing suitable substrates, and minimizing the random potential fluctuations they introduce, has been a persistent challenge in this emerging field. Here we show that Landau-level (LL) spectroscopy offers the unique capability to quantify both the reduction of the quasiparticles' lifetime and the long-range inhomogeneity due to random potential fluctuations. Harnessing this technique together with direct scanning tunneling microscopy and numerical simulations we demonstrate that the insertion of a graphene buffer layer with a large twist angle is a very effective method to shield a 2D system from substrate interference that has the additional desirable property of preserving the electronic structure of the system under study. We further show that owing to its remarkable nonlinear screening capability a single graphene buffer layer provides better shielding than either increasing the distance to the substrate or doubling the carrier density and reduces the amplitude of the potential fluctuations in graphene to values even lower than the ones in AB-stacked bilayer graphene.

graphene | STM | screening | Landau-level spectroscopy

The recent realization of one-atom-thick layers and the fabrication of layered Van der Waals heterostructures revealed fascinating physical phenomena and novel devices based on interlayer interactions (1–10). Inherent to the 2D structure of these layers is an extreme vulnerability to disturbances introduced by the substrate (11–14). Substrate interference can be eliminated by suspending the sample, an approach that led to the observation of ballistic transport (15, 16) and the fractional quantum Hall effect in graphene (17–20), but this method only works for small (micrometer-sized) samples at relatively low doping. Another approach is to use atomically smooth metallic substrates (21–23) or graphite (24–28), which screen the random potential. However, these substrates short-circuit the 2D channel and prevent tuning the carrier density by gating, rendering them unsuitable for device applications. Among insulating substrates atomically flat hBN (29–31) and MoS₂ (6) have recently emerged as promising alternatives to SiO₂ substrates.

Here we show that by inserting a graphene buffer layer between the 2D sample (in this case, also graphene) and the insulating substrate, the random potential fluctuations are screened without compromising the electronic structure of the 2D system under study and the gating capability. This capability relies on the fact that in van der Waals structures the stacking configuration in the third direction can be set arbitrarily and is not fixed by the chemistry of the elements forming the heterostructure. Consequently it is possible to electronically decouple two 2D crystals by simply ensuring that the relative angle (the twist angle) between them is significantly different from values that would lead to a commensurate stacking configuration (2, 30). In this situation the only effect of the additional graphene layer is to screen random potential fluctuations

caused by the substrate. Due to the large twist angle the additional graphene layer (*i*) does not modify the low-energy band structure of the 2D systems under study and (*ii*) does not induce significant intrinsic doping (contrary, for example, to what happens in graphene grown on silicon carbide) and therefore does not compromise the gating capability, which allows probing the intrinsic electronic properties of 2D materials and their doping dependence.

We characterize the reduction of the potential fluctuations in the presence of the additional graphene buffer layer by using direct scanning tunneling microscopy (STM) imaging, spectroscopy (STS), Landau-level (LL) spectroscopy, and numerical simulations. LL spectroscopy gives a measure of the local potential fluctuations by providing access to the onset of well-defined cyclotron orbits, to the quasiparticle lifetime, and to the mean free path. Furthermore, we show that gate-dependent LL spectroscopy allows quantifying the strength of the spatial inhomogeneities induced by the disorder. Using this technique we find that scattering is substantially suppressed in the presence of the graphene buffer layer and that the sample quality is further improved by the proximity to an hBN flake (7). This is the first time to our knowledge that the beneficial effect of introducing a graphene buffer layer is verified and quantified using direct imaging STM, STS mapping of the LLs, and numerical simulations.

Results

Fig. 1A shows the schematic measurement setup. The STM topography of a single layer (GSiO₂) and an adjacent double layer (GGSiO₂) is shown in Fig. 1B. The step height across the boundary between the two regions, ~0.7 nm, is significantly larger than for Bernal stacked graphite (0.34 nm) (32), suggesting that the top and bottom layers are electronically decoupled. Side-by-side topography

Significance

Using scanning tunneling microscopy and numerical simulations we demonstrate that a graphene buffer sheet placed underneath an atomically thin layer is an extremely effective method to increase the quality of 2D electron systems without modifying their electronic structure and without compromising the gating capabilities. We show that owing to its remarkable nonlinear screening capability the graphene buffer layer provides better shielding from substrate-induced perturbations than either increasing the distance to the substrate or doubling the carrier density, or even than using a graphene bilayer.

Author contributions: E.Y.A. designed research; C.-P.L. and A.L.-M. performed research; M.R.-V., G.L., K.W., T.T., and E.R. contributed new reagents/analytic tools; C.-P.L., E.R., and E.Y.A. analyzed data; and E.Y.A. wrote the paper.

Reviewers: J.L., University of California, Riverside; and A.H.M., The University of Texas at Austin.

The authors declare no conflict of interest.

¹Present address: Department of Physics, Ottawa University, Ottawa, ON, Canada K1N 6N5.

²To whom correspondence should be addressed. Email: eandrei@physics.rutgers.edu.

This article contains supporting information online at www.pnas.org/lookup/suppl/doi:10.1073/pnas.1606278113/-DCSupplemental.

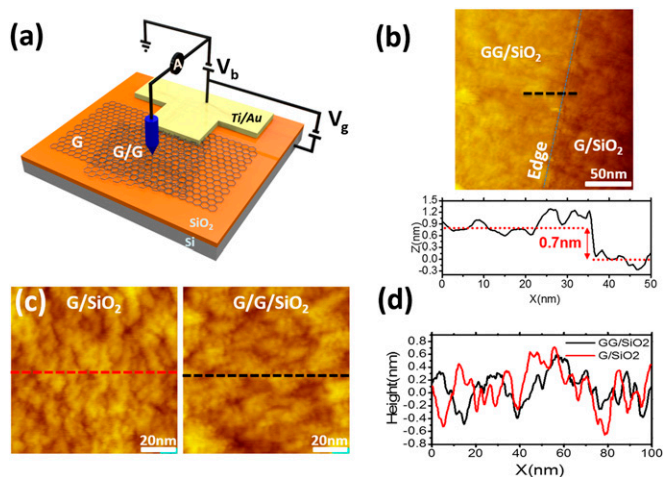


Fig. 1. (A) Schematics of the STM measurement configuration illustrating the G/SiO₂ and GG/SiO₂ samples and the Ti/Au electrode. (B) (Top) Constant current STM topography map of the boundary between GG/SiO₂ and G/SiO₂. (Bottom) Height profile along the dashed line crossing the boundary shows a step height of 0.7 nm. Tunneling parameters: $I_{\text{set}} = 20$ pA and $V_b = 0.7$ V. (C) Constant current STM topographs of G/SiO₂ and GG/SiO₂. Tunneling parameters: $I_{\text{set}} = 20$ pA and $V_b = 0.4$ V. (D) Height profiles along the dashed lines in C.

images on residue-free regions of the G/SiO₂ and GG/SiO₂ samples (Fig. 1C) show that they have the same average height corrugation of ~ 0.9 nm (Fig. 1D). The absence of a moiré pattern in the GG/SiO₂ sample suggests weak interlayer coupling, consistent with their large separation.

Fig. 2A shows the gate voltage, V_g , dependence of the dI/dV spectra for the GG/SiO₂ sample (see Fig. S1 for G/SiO₂). In Fig. 2B we plot the Dirac point (DP) energy, E_D , obtained from Fig. 2A, as a function of V_g . For two decoupled graphene layers, and using the convention where the Fermi energy is at the origin $E_F \equiv 0$, the gate voltage dependence of the DP in the top layer is given by (33) the following: $E_D^t(V_g) = \hbar v_F \sqrt{\nu \pi \alpha |V_g - V_D|}$. Here \hbar is the reduced Planck constant, v_F is the Fermi velocity, $\nu = n_{\text{top}}/n_{\text{total}}$ is the ratio of the carrier density in the top graphene layer (n_{top}) to the total carrier density (n_{total}), $\alpha = 7 \times 10^{10} \text{ cm}^{-2} \cdot \text{V}^{-1}$ is the charging capacitance per layer, per unit area and unit charge, and V_D indicates the gate voltage needed to cancel the unintentional doping. To obtain the charge distribution between the two layers we use the value of v_F independently measured from LL spectroscopy as discussed below. Fitting the data in Fig. 2A to this expression with $v_F = 1.12 \times 10^6$ m/s, we obtain $\nu = 0.43$, indicating that the top layer is slightly less populated than the bottom one. In addition, we find $V_D = 22.5 \pm 0.5$ V, corresponding to unintentional hole doping with an average carrier density, n , of $\sim 8 \times 10^{11} \text{ cm}^{-2}$. The substrate-induced random potential produces electron-hole puddles observed as density of states (DOS) fluctuations in the maps shown in Fig. 2C and D for G/SiO₂ and GG/SiO₂, respectively. The substantial reduction of the fluctuations in GG/SiO₂ compared with G/SiO₂ reflects the significant screening afforded by the buffer graphene layer.

To understand screening in this system we carried out numerical simulations that used the Thomas–Fermi–Dirac theory (TFDT) (34, 35). In graphene, unlike the case of materials with parabolic bands, the disorder potential created by trapped charges retains its long-range nature (36–38). This property, together with the nonlinear nature of the screening in graphene (34, 39), poses significant challenges to theoretical treatments. Previous work has shown that TFDT provides a computationally feasible approach to modeling this problem (*Supporting Information, Notes on Modeling Puddles in the Graphene–Graphene System*).

Starting from the random distribution of charge impurities shown in Fig. S2A and B we used TFDT to numerically illustrate the screening effect of a single graphene layer (Fig. 2E) and to demonstrate the shielding effect of adding a second layer (Fig. 2F). Similarly to the experimental results, we find that the double layer experiences a substantial reduction in the potential fluctuations compared with the single layer. This reduction cannot be explained simply as a consequence of higher carrier density, or the larger distance from the SiO₂ plane (39), as clearly shown in Fig. 3, where we compare the strength of the potential fluctuations in single- and double-layer graphene. We see that neither an increase of the distance from the substrate, d , nor a doubling of the carrier density is sufficient to reduce the strength of the fluctuations in the single layer to the values obtained, and observed experimentally, for the double layer. Remarkably, as shown in Fig. 3B, even in the limit in

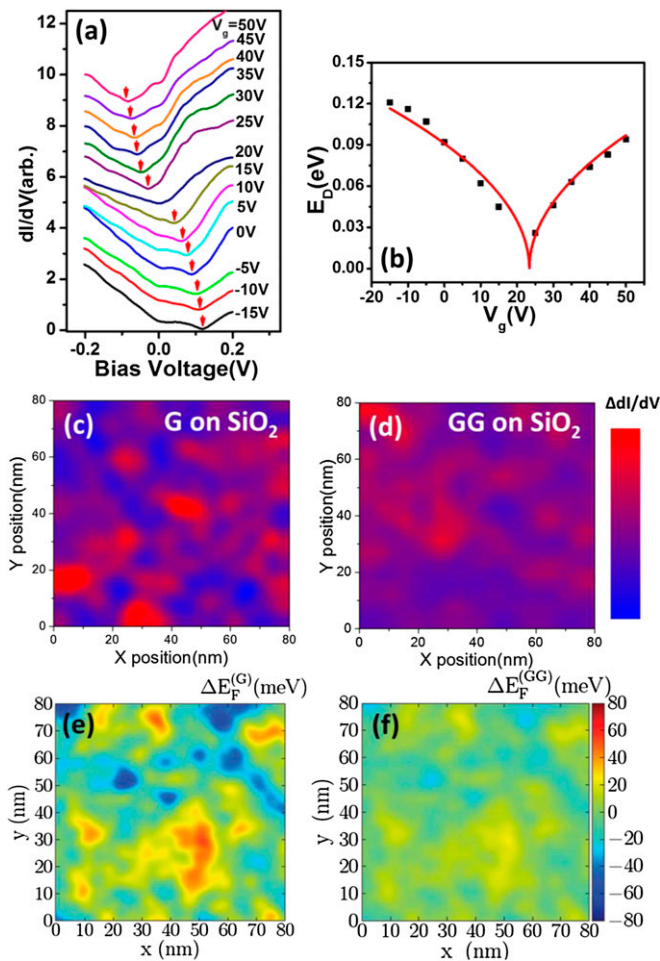


Fig. 2. (A) Gate voltage dependence of dI/dV spectra on GG/SiO₂. Curves are vertically displaced for clarity. Red arrows indicate the conductance minimum which is identified with E_D . Tunneling parameters: $I_{\text{set}} = 20$ pA, $V_b = 0.3$ V, and modulation voltage 5 mV. (B) Gate voltage dependence of measured E_D (squares) together with the fit (solid line) discussed in the text. (C and D) dI/dV maps at $V_b = 0.3$ V reveal the electron (red) hole (blue) puddles resulting from doping inhomogeneity. Maps cover the same areas as in Fig. 1C. The color scale, which is proportional to the deviation of dI/dV from the mean value across the map, is a direct representation of the local fluctuations of E_D . (E and F) Simulated map illustrating the spatial fluctuations of E_D for a single disorder realization (shown in Fig. S3A and B) for a graphene single layer (E) and double layer (F). Simulation parameters: impurity density $n_{\text{imp}} = 5 \times 10^{11} \text{ cm}^{-2}$, carrier density $\langle n \rangle = 1 \times 10^{12} \text{ cm}^{-2}$, average distance d between the charge impurities and the graphene layer closest to the substrate 1.5 nm, and interlayer distance 0.7 nm.

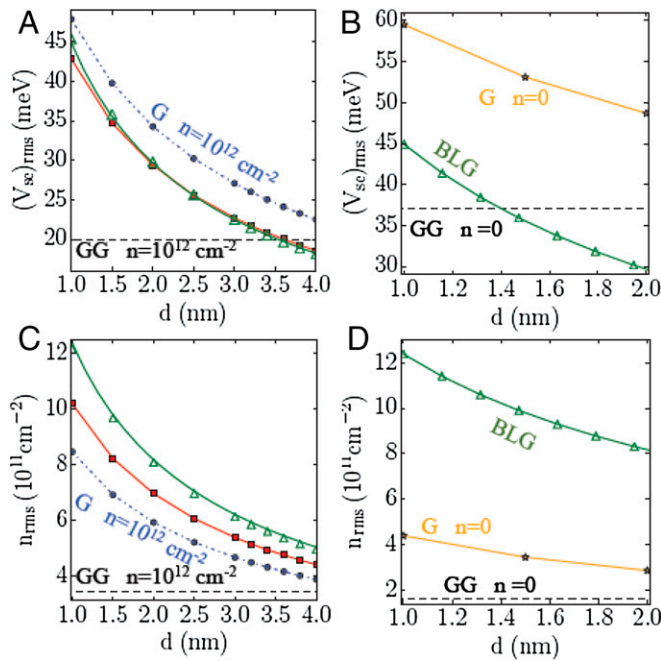


Fig. 3. Comparison of the potential fluctuations in single graphene (G), BLG, and double graphene (GG) obtained using the TFDT. In each panel the black dashed line shows the values obtained for GG assuming $d = 1.5$ nm, $n = 10^{12}$ cm $^{-2}$, and $n_{\text{imp}} = 5 \times 10^{11}$ cm $^{-2}$. (A) The dependence of the rms of the potential fluctuations (i.e., of E_D) as a function of the distance d between the graphene layer and the impurities. The dashed blue lines show the results for G with doping $n = 10^{12}$ cm $^{-2}$, and the solid red lines the results for G with doping $n = 2 \times 10^{12}$ cm $^{-2}$. The solid green lines show the analytic results for BLG (Supporting Information), and the green empty triangles show the results for BLG obtained using the TFDT. Neither an increase of d , nor a doubling of the carrier density, is sufficient to reduce the fluctuations to the levels seen in GG. In BLG, at low dopings, the rms of the screened disorder and of the carrier density fluctuations does not depend on the doping. From the figure we see that only when d is very large, the strength of the disorder-induced fluctuations is larger in GG (for a doping $n = 10^{12}$ cm $^{-2}$) than in BLG. (B) Even when the Fermi level is set at the Dirac point, the potential fluctuations are much smaller in GG than in G. (C and D) The rms of the carrier density fluctuations corresponding to A and B, respectively.

which the doping is set at the Dirac point, in both layers, the random potential fluctuations are substantially reduced. For comparison we also show the case of an AB-stacked bilayer graphene (BLG), where we find that in the regime relevant to the current experiments the strength of the disorder-induced fluctuations is significantly larger than in the double-layer case. At high doping the graphene buffer layer reduces the potential fluctuations in the top graphene layer to values even lower than the ones of the BLG, mainly because of its higher DOS compared with the almost constant DOS of AB bilayer graphene. However, even at the charge neutrality point for $d \lesssim 1.5$ nm the graphene buffer layer can reduce the potential fluctuations to values smaller than in BLG. The reason for the unusually strong screening efficiency of the graphene buffer layer is the nonlinear screening inherent to the linear dispersion of the charge carriers in single-layer graphene. Owing to this nonlinearity large potential fluctuations are screened more efficiently than smaller ones, with the net effect of flattening the random potential landscape.

LL spectroscopy makes it possible to quantify the screening effect by providing access to the quasiparticle lifetime and the random potential fluctuations (27, 28). In the presence of a magnetic field, B , normal to the layer the spectrum breaks up into a sequence of LLs (40):

$$E_N = E_D \pm \frac{\hbar v_F}{l_B} \sqrt{2|N|} \quad N = 0, \pm 1, \pm 2, \pm 3, \dots, \quad [1]$$

where $l_B = (\hbar/eB)^{1/2}$ is the magnetic length and e the fundamental unit of charge. The LLs become observable when their characteristic energy separation, $v_F \sqrt{2e\hbar B}(\sqrt{N+1} - \sqrt{N})$, exceeds the linewidth, ΔE , whose magnitude is primarily controlled by the random potential fluctuations. This property defines an onset field, $B_o \sim (\frac{\Delta E}{v_F})^2 \frac{1}{2e\hbar}$, above which the first LL becomes observable, whereas for $B < B_o$ the behavior is dominated by scattering from the random potential. Thus, B_o measures the local random potential fluctuations, providing a gauge of substrate quality. $B > B_o$ implies $l_B < l$, where $l = v_F \tau_i$ is the mean free path and τ_i is the transport time. For the regimes considered τ_i is of the order (apart from a coefficient of order 1) of the quasiparticle lifetime (41) $\tau \approx \hbar/\Delta E$. In other words, LLs become observable when the magnetic length is smaller than the mean free path.

The evolution of LLs with field for the GSiO $_2$ and GGSiO $_2$ samples is shown in Fig. 4 A and B, respectively. In both samples the LL energies follow the $E_N \propto \sqrt{|N|B}$ dependence expected for single-layer graphene (Fig. S44). Fitting the data to Eq. 1 we find $v_F = (1.10 \pm 0.1) \times 10^6$ m/s and $(1.12 \pm 0.1) \times 10^6$ m/s for the single and double layer, respectively. Both values are consistent with the accepted value for single-layer graphene on SiO $_2$, as expected for complete decoupling of top and bottom layers. The LL peaks in GGSiO $_2$ are sharper and their onset is earlier than in GSiO $_2$, indicating a more homogeneous charge distribution and a longer quasiparticle lifetime. Gaussian fits of the $n = 0$ LL (Fig. S4) give $\Delta E \sim 42$ meV and 18 meV for the single and double layer, respectively, corresponding to more than doubling the carrier lifetimes, from $\tau \approx 15$ fs to $\tau \approx 35$ fs and to a similar increase in the mean free path from $l \sim 15$ nm to ~ 35 nm. Estimating the onset fields from the linewidths we find $B_o \sim 3$ T and $B_o \sim 0.5$ T for the single and double layer, respectively, consistent with the data. These results show that the buffer graphene layer significantly reduces the local potential fluctuations. Using TFDT simulations with the same parameters as those in Fig. 2 E and F to calculate the disorder averaged values of the random potential fluctuations, we find for the rms of the potential fluctuations, $\Delta E = 40$ meV and 20 meV for single and double layer, respectively, in agreement with the experimental values (Supporting Information, Notes on Modeling Puddles in the Graphene-Graphene System and Fig. 3A). It is worth noting that the contribution to the linewidth from electron-electron interactions for samples supported on SiO $_2$ is negligible compared with that from the random potential (27). This extrinsic scattering mechanism is consistent with the fact that the LL lineshape is Gaussian and the linewidth is independent of energy. In contrast, for the case of graphene on graphite (25–28) where scattering is intrinsic, the lineshape is Lorentzian and the linewidth, which increases linearly with energy, is almost an order of magnitude narrower than here.

In Fig. 4C we illustrate the effect of an hBN flake placed close to the double layer (Fig. S54). The onset field, ~ 0.5 T, and the linewidth, $\Delta E_l \sim 17$ meV, are not very different from the case without the hBN flake. However, as we show next, even though it is not part of the graphene substrate the mere proximity of the hBN suppresses the global potential fluctuations. This suppression is consistent with earlier reports of self-cleansing at the graphene-hBN interface, which is believed to segregate contaminants, leaving the rest of the interface atomically clean (7).

We have seen that the LL linewidth gives the scale of the mean free path and therefore the scale of the rms of the potential fluctuations. Next we show that the evolution of LL spectra with the gate voltage also provides access to the maximum strength of the global disorder-induced potential fluctuations across the entire sample. In the absence of fluctuations the gate dependence of the LLs produces a staircase pattern consisting of a sequence of

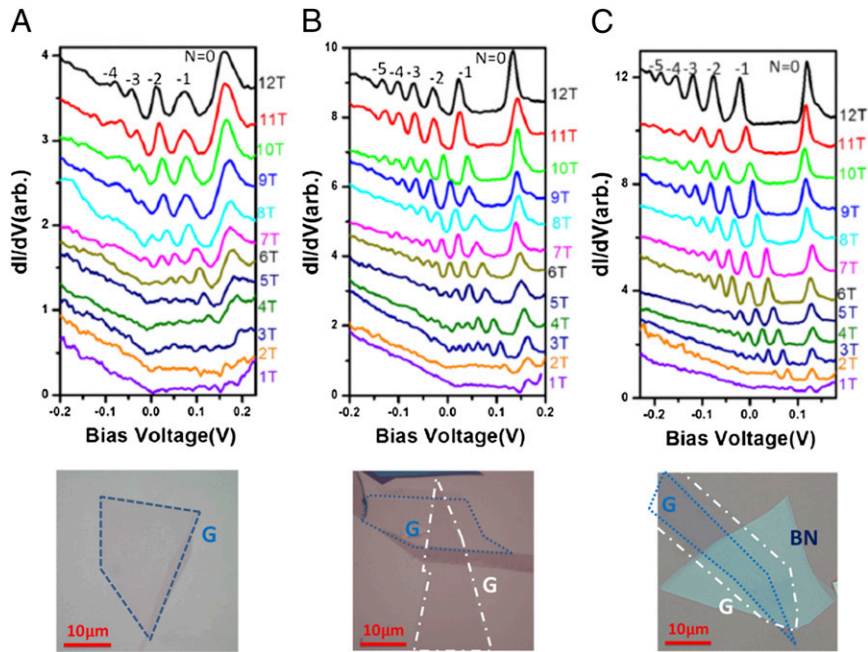


Fig. 4. Magnetic field dependence of LL spectra. (A) GSiO₂, $V_g = 10$ V. (B) GGSiO₂, $V_g = -15$ V. (C) GGSiO₂ in the vicinity of hBN, $V_g = -10$ V. All curves are offset vertically for clarity. The LL indexes, $n = 0, -1, -2, -3, \dots$, are marked. The optical micrograph of the measured sample is shown in the bottom inset of each panel. The blue and white dashed lines represent the outline of the bottom and top graphene layers, respectively. STS parameters: $I_{\text{set}} = 20$ pA, sample bias $V_b = 0.3$ V, and modulation voltage 2 mV.

equidistant plateaus separated by sharp jumps (42, 43). The plateaus reflect the pinning of E_F within an LL as it is being filled, and their width, $\Delta V_g = \frac{8}{\alpha} \frac{B}{\phi_0}$, corresponds to the gate voltage needed to populate all available states in one LL (a total of $8 \frac{B}{\phi_0}$) (43). Here $\phi_0 = 4.14 \times 10^{-15}$ Tm² is the fundamental unit of flux and 8 reflects the degeneracy due to spin, valley, and two layers. Once the N th LL is filled, E_F jumps to the next LL, producing the sharp step. Note that because E_F defines the energy origin, it is E_D and the LLs that seem to be shifting, rather than E_F .

A random potential smears out the staircase structure because E_D (and the entire LL sequence with it) fluctuates across the sample following the potential variations as illustrated in Fig. 5A. It is important to note that V_g , being controlled by the gate electrode, deposits charge across the entire area of the sample and not only at the position of the STM tip. Therefore, as V_g is swept the first electron to populate a given LL will occupy a state localized near the global minimum of the random potential whereas the last electron will find a state near the global maximum, neither of which is necessarily close to the tip position. However, the effect of filling these states is felt, even when they are far from the tip, through the global shift in E_F , which is seen as a shift in the $n = 0$ LL (i.e., the local value of E_D). As states are being populated and E_F gradually increases, the spectrum measured by the STM tip shifts down in energy, causing the LL energy to trace out the random potential fluctuation, ΔE_G . The total downshift of the plateau as it is being populated provides a measure of the maximum strength of the disorder-induced potential fluctuations.

In Fig. 5B–D we show the gating effect on the LL spectra for GSiO₂, GGSiO₂, and GGSiO₂ near hBN, respectively. In the case of GSiO₂ the absence of an observable staircase structure signifies that ΔE_G exceeds the LL spacing at 10 T ~ 115 meV ~ 3 rms, taking rms ~ 42 meV as obtained from the onset field. For the GGSiO₂ sample the staircase becomes discernible and from the plateau slope we find $\Delta E_G \sim 50$ meV. Thus, adding a second graphene layer strongly suppresses the substrate-induced disorder on both local and global scales. Most remarkably, when the sample is close to an hBN flake the global potential fluctuations are almost completely suppressed, as shown in Fig. 5C and

also Fig. S5B and C. Now the plateaus are much flatter with an estimated slope of ~ 11 meV, corresponding to a reduction of ΔE_{DG} below the LL linewidth, directly demonstrating the efficacy of the self-cleansing phenomenon of hBN.

Discussion

An interesting question for further study is how the screening properties depend on the degree of coupling between the two graphene layers. When the twist angle θ between the layers is such that the two layers are in a commensurate (or almost commensurate) stacking configuration the coupling between the two layers is increased. In this situation, when θ is such that the primitive cell of the commensurate structure has dimensions much larger than the graphene lattice spacing, a Moiré pattern emerges, and Van Hove singularities appear in the DOS at energies separated by the energy interval $\Delta E_{VHS} = 2K\hbar v_F \sin(\theta/2)$, where K is the magnitude of the vectors that identify the corners of the graphene Brillouin zone. For sufficiently large twist angles, and large primitive cells, therefore the low-energy band structure is unaffected by the second layer. Given that for large twist angles, and large primitive cells, the coupling between the layers only affects the high-energy states, one expects that for low-energy probes, such as transport measurements, the screening benefit of a second layer would still apply, and that only high-energy probes, such as optical measurements, will be sensitive to the effects of the interlayer coupling on the bands of the double layer. For the samples discussed here, the absence of a Moiré pattern indicates that the layers are electronically decoupled without appreciable tunneling between them. This conclusion is confirmed by the fact that the local DOS in the top layer is not altered by the presence of the lower layer, apart from the reduction in disorder. In this regime we only have incoherent random tunneling processes between the two layers. Such random tunneling processes simply induce a broadening of the quasiparticle states that for most conditions is negligible compared with the broadening induced by the disorder. As a consequence, the tunneling-induced broadening does not affect the transport properties. Early transport measurements (44) and LL spectroscopy (33, 45) have shown that the

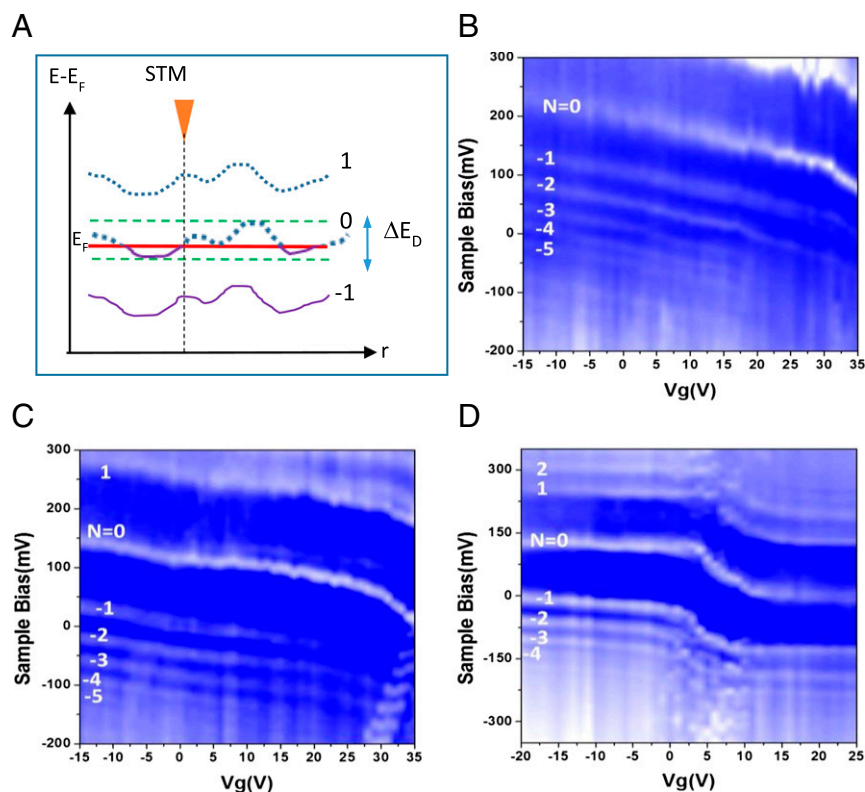


Fig. 5. Gate dependence of LL spectra. (A) Schematic illustration of the effect of global random potential on the spatial dependence of the LLs for $n = 0, \pm 1$. Filled (empty) LL states below (above) the Fermi energy (horizontal red line) are marked by solid (dotted) lines. The position of the STM tip is marked by the arrow. ΔE_D represents the fluctuation of the LL energy across the entire sample. (B) Gate voltage maps of LLs at 10 T for the GSiO₂ sample. Each vertical line represents an LL spectrum at a particular V_g . (C and D) Same as B for GGSiO₂ and GGSiO₂ in the vicinity of hBN, respectively. The LL indexes, $n = 0, \pm 1, \pm 2, \dots$, are marked. STS parameters: $I_{\text{set}} = 20$ pA, sample bias $V_0 = 0.3$ V, and modulation voltage 5 mV.

population of the electronic states in the two layers depends on the displacement field, D , between them. For the samples studied here the carrier density is almost evenly distributed between the two layers. Deviations from $D = 0$, which can be due to unintentional doping or can be induced with a top gate, cause a charge imbalance between the layers and a corresponding shift between the two charge neutrality points, but more experiments are needed to understand how this imbalance affects the screening properties.

In summary this work demonstrates that, owing to its nonlinear screening properties, a graphene buffer sheet placed underneath an atomically thin layer substantially reduces random potential fluctuations introduced by a substrate. We show that this is an extremely effective and simple method to increase the quality of 2D electron systems without modifying their electronic structure and without compromising the gating capabilities. This is the first work, to our knowledge, showing a direct comparison between theory and experiment that quantitatively characterizes the role of electron-hole puddles, and demonstrates an efficient way to suppress their deleterious effects in graphene heterostructures.

Methods

Devices were fabricated from exfoliated graphene flakes and transferred onto the surface of a 300-nm chlorinated SiO₂ layer capping a highly n-doped Si substrate, which served as a back gate. To ensure decoupling between the top and bottom graphene layers and to avoid interference from Van Hove singularities (2, 3, 46), the layers were deposited with a large twist angle between them. Standard e-beam lithography followed by electron-beam evaporation at base pressure of 2×10^{-7} Torr was used to deposit the Ti/Au (2 nm/60 nm) pads for guiding the STM tip to the sample (47). The devices were baked for 3 h in forming gas at 250 °C before mounting into the cryostat. STM and STS measurements were performed at 4 K in a home-built STM using Pt-Ir tips that were mechanically cut from polycrystalline wire. STM images were recorded in constant current mode with the bias voltage, V_b , applied between the sample and grounded tip. Differential conductance (dI/dV) spectra, which are proportional to the local DOS, were obtained with a lock-in technique at modulation frequency 440 Hz with fixed tip to sample distance.

ACKNOWLEDGMENTS. We thank Ivan Skachko and Jinhai Mao for useful discussions. Funding was provided by Department of Energy Grant DOE-FG02-99ER45742, National Science Foundation (NSF) Grants DMR 1207108 and EFRI-2DARE 1433307, and NSF CAREER DMR-1455233 and ACS-PRF 53581-DNI5 (to M.R.-V. and E.R.).

- Geim AK, Grigorieva IV (2013) Van der Waals heterostructures. *Nature* 499(7459): 419–425.
- Li G, et al. (2010) Observation of Van Hove singularities in twisted graphene layers. *Nat Phys* 6(2):109–113.
- Luican A, et al. (2011) Single-layer behavior and its breakdown in twisted graphene layers. *Phys Rev Lett* 106(12):126802.
- Bistritzer R, MacDonald AH (2011) Moire bands in twisted double-layer graphene. *Proc Natl Acad Sci USA* 108(30):12233–12237.
- Lee GH, et al. (2013) Flexible and transparent MoS₂ field-effect transistors on hexagonal boron nitride-graphene heterostructures. *ACS Nano* 7(9):7931–7936.
- Lu CP, Li G, Watanabe K, Taniguchi T, Andrei EY (2014) MoS₂ MoS₂: Choice substrate for accessing and tuning the electronic properties of graphene. *Phys Rev Lett* 113(15):156804.
- Kretinin AV, et al. (2014) Electronic properties of graphene encapsulated with different two-dimensional atomic crystals. *Nano Lett* 14(6):3270–3276.
- Zhang J, Triola C, Rossi E (2014) Proximity effect in graphene-topological-insulator heterostructures. *Phys Rev Lett* 112(9):096802.
- Bian G, et al. (2015) Experimental observation of two massless Dirac-Fermion gases in graphene-topological insulator heterostructure. arXiv:1511.02413.
- Steinberg H, et al. (2015) Tunneling in graphene topological insulator hybrid devices. *Phys Rev B* 92(24):241409.
- Ishigami M, Chen JH, Cullen WG, Fuhrer MS, Williams ED (2007) Atomic structure of graphene on SiO₂. *Nano Lett* 7(6):1643–1648.
- Martin J, et al. (2008) Observation of electron-hole puddles in graphene using a scanning single-electron transistor. *Nat Phys* 4(2):144–148.

13. Geringer V, et al. (2009) Intrinsic and extrinsic corrugation of monolayer graphene deposited on SiO₂. *Phys Rev Lett* 102(7):076102.
14. Zhang YB, Brar VW, Girit C, Zettl A, Crommie MF (2009) Origin of spatial charge inhomogeneity in graphene. *Nat Phys* 6(1):722–726.
15. Du X, Skachko I, Barker A, Andrei EY (2008) Approaching ballistic transport in suspended graphene. *Nat Nanotechnol* 3(8):491–495.
16. Bolotin KI, et al. (2008) Ultrahigh electron mobility in suspended graphene. *Solid State Commun* 146:351–355.
17. Du X, Skachko I, Duerr F, Luican A, Andrei EY (2009) Fractional quantum Hall effect and insulating phase of Dirac electrons in graphene. *Nature* 462(7270):192–195.
18. Bolotin KI, Ghahari F, Shulman MD, Stormer HL, Kim P (2009) Observation of the fractional quantum Hall effect in graphene. *Nature* 462(7270):196–199.
19. Abanin DA, Skachko I, Du X, Andrei EY, Levitov LS (2010) Fractional quantum Hall effect in suspended graphene: Transport coefficients and electron interaction strength. *Phys Rev B* 81(11):115410.
20. Bao W, et al. (2010) Magnetoconductance oscillations and evidence for fractional quantum Hall states in suspended bilayer and trilayer graphene. *Phys Rev Lett* 105(24):246601.
21. Land TA, Michely T, Behm RJ, Hemminger JC, Comsa G (1992) STM investigation of single layer graphite structures produced on Pt(111) by hydrocarbon decomposition. *Surf Sci* 264(3):261–270.
22. Marchini S, Günther S, Wintterlin J (2007) Scanning tunneling microscopy of graphene on Ru(0001). *Phys Rev B* 76(7):075429.
23. Coraux J, N'Diaye AT, Busse C, Michely T (2008) Structural coherency of graphene on Ir(111). *Nano Lett* 8(2):565–570.
24. Li G, Andrei EY (2007) Observation of Landau levels of Dirac fermions in graphite. *Nat Phys* 3(9):623–627.
25. Li G, Luican A, Andrei EY (2009) Scanning tunneling spectroscopy of graphene on graphite. *Phys Rev Lett* 102(17):176804.
26. Neugebauer P, Orlita M, Faugeras C, Barra A-L, Potemski M (2009) How perfect can graphene be? *Phys Rev Lett* 103(13):136403.
27. Andrei EY, Li G, Du X (2012) Electronic properties of graphene: A perspective from scanning tunneling microscopy and magnetotransport. *Rep Prog Phys* 75(5):056501.
28. Luican A, Li G, Andrei EY (2009) Scanning tunneling microscopy and spectroscopy of graphene layers on graphite. *Solid State Commun* 149(27–28):1151–1156.
29. Dean CR, et al. (2011) Multicomponent fractional quantum Hall effect in graphene. *Nat Phys* 7(9):693–696.
30. Xue J, et al. (2011) Scanning tunneling microscopy and spectroscopy of ultra-flat graphene on hexagonal boron nitride. *Nat Mater* 10(4):282–285.
31. Decker R, et al. (2011) Local electronic properties of graphene on a BN substrate via scanning tunneling microscopy. *Nano Lett* 11(6):2291–2295.
32. Niimi Y, et al. (2006) Scanning tunneling microscopy and spectroscopy of the electronic local density of states of graphite surfaces near monoatomic step edges. *Phys Rev B* 73:085421.
33. Mao J, et al. (2016) Realization of a tunable artificial atom at a supercritically charged vacancy in graphene. *Nat Phys*, 10.1038/nphys3665.
34. Rossi E, Das Sarma S (2008) Ground state of graphene in the presence of random charged impurities. *Phys Rev Lett* 101(16):166803.
35. Rodríguez-Vega M, Fischer J, Das Sarma S, Rossi E (2014) Ground state of graphene heterostructures in the presence of random charged impurities. *Phys Rev B* 90:035406.
36. Das Sarma S, Adam S, Hwang EH, Rossi E (2011) Electronic transport in two-dimensional graphene. *Rev Mod Phys* 83(2):407–470.
37. Nomura K, MacDonald AH (2006) Quantum Hall ferromagnetism in graphene. *Phys Rev Lett* 96(25):256602.
38. Hwang EH, Adam S, Sarma SD (2007) Carrier transport in two-dimensional graphene layers. *Phys Rev Lett* 98(18):186806.
39. Kuroda MA, Tersoff J, Martyna GJ (2011) Nonlinear screening in multilayer graphene systems. *Phys Rev Lett* 106(11):116804.
40. Castro Neto AH, Guinea F, Peres NMR, Novoselov KS, Geim AK (2009) The electronic properties of graphene. *Rev Mod Phys* 81(1):109.
41. Hwang EH, Das Sarma S (2008) Single-particle relaxation time versus transport scattering time in a two-dimensional graphene layer. *Phys Rev B* 77(19):195412.
42. Dial OE, Ashoori RC, Pfeiffer LN, West KW (2007) High-resolution spectroscopy of two-dimensional electron systems. *Nature* 448(7150):176–179.
43. Luican A, Li G, Andrei EY (2011) Quantized Landau level spectrum and its density dependence in graphene. *Phys Rev B* 83:041405.
44. Sanchez-Yamagishi JD, et al. (2012) Quantum Hall effect, screening, and layer-polarized insulating states in twisted bilayer graphene. *Phys Rev Lett* 108(7):076601.
45. Luican-Mayer A, et al. (2014) Screening charged impurities and lifting the orbital degeneracy in graphene by populating Landau levels. *Phys Rev Lett* 112(3):036804.
46. Brihuega I, et al. (2012) Unraveling the intrinsic and robust nature of van Hove singularities in twisted bilayer graphene by scanning tunneling microscopy and theoretical analysis. *Phys Rev Lett* 109(19):196802.
47. Li G, Luican A, Andrei EY (2011) Self-navigation of an STM tip toward a micron sized sample. *Rev Sci Instrum* 82(7):073501.
48. Shklovskii BI, Efros AL (1984) *Electronic Properties of Doped Semiconductors* (Springer, New York).
49. Efros ALF, Pikus FG, Burnett VG (1993) Density of states of a two-dimensional electron gas in a long-range random potential. *Phys Rev B Condens Matter* 47(4):2233–2243.
50. Polini M, Tomadin A, Asgari R, MacDonald AH (2008) Density-functional theory of graphene sheets. *Phys Rev B* 78:115426.
51. Rossi E, Adam S, Das Sarma S (2009) Effective medium theory for disordered two-dimensional graphene. *Phys Rev B* 79(24):245423.
52. Rossi E, Das Sarma S (2011) Inhomogeneous electronic structure, transport gap, and percolation threshold in disordered bilayer graphene. *Phys Rev Lett* 107(15):155502.

Supporting Information

Lu et al. 10.1073/pnas.1606278113

Gate Voltage Dependence of GSiO₂ Sample

Fig. S1A shows the dI/dV measurements of graphene on SiO₂ for different gate voltages. Red arrows indicate the conductance minimum that is identified with E_D . In Fig. S1B we have Gate-voltage dependence of E_D for graphene on the chlorinated SiO₂ substrate. The solid line represents a fit of the massless Dirac fermion spectrum of graphene to the data:

$$E_D = \hbar v_F \sqrt{\pi \alpha |V_G - V_0|}.$$

Here \hbar is the reduced Planck constant. The offset $V_0 \sim 12$ V and the Fermi velocity $v_F = 1.1 \pm 0.02 \times 10^6$ m/s are obtained from the fitting of LL spectra.

Notes on Modeling Puddles in the Graphene–Graphene System

There is compelling evidence that in graphene-based systems, especially when the substrate is SiO₂, charge impurities are the dominant source of disorder (36). In graphene-based systems the Coulomb nature of the disorder makes its theoretical treatment challenging. This difficulty is due to the linear nature of graphene's low-energy bands, which implies that in graphene, differently than in a standard 2D electron gas with parabolic bands, or a metal, the disorder potential created by charge impurities retains its long-range nature even when screening effects are taken into account (36–38) and that, in addition, nonlinear screening effects are very important and must be taken into account (34).

The long-range nature of the disorder and the necessity to take into account nonlinear screening effects make the use of standard diagrammatic methods to describe the effect of disorder unsuitable. In this situation functional methods are much more effective (48, 49). In principle, one could use density functional theory (DFT). However, the fact that the disorder breaks the periodicity of the system makes the use of DFT computationally very expensive and possible only for small size (few nanometers) systems (50). An approach similar in spirit to DFT, but computationally much less expensive, is the TFDT (34). In this approach, contrary to DFT, also the kinetic energy operator is replaced by a functional of the density, $E_K[n]$, appropriate for the case in which the electronic degrees of freedom behave as massless Dirac fermions, as in single-layer graphene.

The presence of long-range disorder causes the appearance of long-range carrier density inhomogeneities (36). The TFDT returns accurate results as long as the length scale of the carrier density inhomogeneities $|\nabla n/n|^{-1}$ is larger than the Fermi wavelength λ_F . Due to the long-range nature of the inhomogeneities it is possible to define a local λ_F (51). For samples for which the impurity density n_{imp} is larger than 10^{11} cm^{-2} the local density, even at the charge neutrality point, is large enough to satisfy the condition for the validity of the TFDT.

For a structure comprising two graphene layers the TFDT energy functional takes the form (35)

$$\begin{aligned} E[n_i] = & \sum_i E_K[n_i] + \sum_i \frac{e^2}{2\epsilon} \int d^2r \int d^2r' \frac{n_i(\mathbf{r})n_i(\mathbf{r}')}{|\mathbf{r}-\mathbf{r}'|} \\ & + \sum_{i,j \neq i} \frac{e^2}{2\epsilon} \int d^2r \int d^2r' \frac{n_i(\mathbf{r})n_j(\mathbf{r}')}{[|\mathbf{r}-\mathbf{r}'|^2 + d^2]^{1/2}} \\ & + e \sum_i \int d^2r V_D^i(\mathbf{r})n_i(\mathbf{r}) - \sum_i \mu_i \int d^2r n_i(\mathbf{r}), \quad \text{[S1]} \end{aligned}$$

where $n_i(\mathbf{r})$ is the carrier density profile in graphene layer i , ϵ is the dielectric constant of the medium surrounding the graphenic

layers, d_{12} is the distance between the graphenic layers, V_D^i is the bare disorder potential in layer i , and μ_i is the chemical potential in layer i . The second and third terms in Eq. S1 represent, respectively, the intralayer and interlayer Hartree part of the Coulomb interaction. Assuming that charge impurities close to the surface of SiO₂ are the dominant source of disorder we have

$$V_D^{(1)} = \frac{e}{\epsilon} \int d\mathbf{r}' \frac{c(\mathbf{r}')}{[|\mathbf{r}-\mathbf{r}'|^2 + d^2]^{1/2}} \quad \text{[S2]}$$

$$V_D^{(2)} = \frac{e}{\epsilon} \int d\mathbf{r}' \frac{c(\mathbf{r}')}{[|\mathbf{r}-\mathbf{r}'|^2 + (d+d_{12})^2]^{1/2}}, \quad \text{[S3]}$$

where $c(\mathbf{r})$ is the distribution of charge impurities. Here we have denoted with $i = 1$ the layer closest to the substrate. To minimize the number of parameters entering the theory $c(\mathbf{r})$ is taken to be effectively a 2D distribution placed at a distance d below the surface of the dielectric substrate. Using angle brackets to denote quantities averaged over the whole sample, without loss of generality, we can assume $\langle c(\mathbf{r}) \rangle = 0$. We also assume the impurities to be uncorrelated so that $\langle c(\mathbf{r})c(\mathbf{r}') \rangle = n_{\text{imp}}\delta(\mathbf{r}-\mathbf{r}')$.

The ground state density profiles $\{n_j(\mathbf{r})\}$ are obtained by minimizing the functional $E[n_j]$, that is, by solving the two coupled equations resulting from setting $\delta E/\delta n_i = 0$. In graphene, the term

$$\delta E_K/\delta n = \mu_{\text{kin}}[n] = \hbar v_f \text{sign}(n(\mathbf{r}))\sqrt{\pi|n(\mathbf{r})|} \quad \text{[S4]}$$

introduces a nonlinear term in the equations that forces us to solve the TFDT equations numerically. After obtaining the density profiles, using Eq. S4 the profiles of the local Fermi energy, or equivalently, of the local shift of the Dirac point, are obtained.

To quantify the effect of the graphene buffer layer in a statistically significant way we calculate the disorder-averaged value of the rms of ΔE_F , that is, the value of ΔE_F averaged over several samples having the same parameter values (impurity density, doping, ...) but different spatial positions of the impurities. Due to its computational efficiency, the TFDT allows the calculation of the disorder-averaged quantities. Using samples 160×160 nm we have calculated the disorder averaged values of the rms of ΔE_F using $N_{\text{samples}} = 600$ disorder realizations (we find that that for $N_{\text{samples}} \geq 500$ the disorder averaged values remain unchanged if we consider more disorder realizations). For the parameters used to obtain the results shown in Fig. 2 E and F and Fig. S2 A and B we find the disorder averaged probability distributions $P(\Delta E_F)$ of ΔE_F shown in Fig. S2 C and D for G and GG, respectively. We see that for the top graphene layer of GGSiO₂ $P(\Delta E_F)$ is much narrower than for GSiO₂, a reflection of the lower amplitude of the carrier density inhomogeneities. From these probability distributions we obtain that the value of the rms of ΔE_F is equal to 40 meV for GSiO₂ and to 20 meV for GGSiO₂.

Using the TFDT we have also characterized the disorder-induced fluctuations in BLG and compared them with the GG case. To obtain the carrier density profile in BLG in the presence of charge impurities one must take into account that the random field created by the charge impurities can induce the opening of a band gap. Using the TFDT we have found that for the conditions relevant for the experiment ($n < 10^{12} \text{ cm}^{-2}$) the small random gap induced by the impurities does not affect in any quantitative

way the values of the carrier density rms, n_{rms} , and screened disorder potential rms, $(V_{sc})_{rms}$. For n_{rms} and $(V_{sc})_{rms}$ we can then use the values obtained when there is no band gap (52):

$$n_{rms} = \frac{\sqrt{n_{imp}}}{r_{sc}} \sqrt{\frac{2}{\pi}} f(d/r_{sc})$$

$$(V_{sc})_{rms} = \frac{\hbar^2 \pi}{2m^*} n_{rms},$$

where $f(d/r_{sc}) = e^{\frac{2d}{r_{sc}}} \left(1 + \frac{2d}{r_{sc}}\right) \Gamma\left(0, \frac{2d}{r_{sc}}\right) - 1$ is a dimensionless function, $r_{sc} = \frac{\epsilon \hbar^2}{2e^2 m^*} \sim 2$ nm is the screening length (with ϵ the dielectric constant, e the electron's charge, and m^* the effective mass), and $\Gamma(a, x)$ is the incomplete gamma function. Notice that to very good approximation in BLG n_{rms} and $(V_{sc})_{rms}$ do not depend on the value of the doping, contrary to the case of double-layer graphene. Fig. 3 B and D show the comparison of the values of n_{rms} and $(V_{sc})_{rms}$ in BLG and GG. From this figure we see that for the doping levels of the double layer relevant for the current experiment and values of $d \lesssim 1.5$ the disorder-induced fluctuations are weaker in GG than in BLG.

Fig. S3 A and B show the disorder averaged rms of the carrier density fluctuations and screened disorder potential as a function of d for different values of the impurity density for G (dashed lines) and GG (solid lines). Fig. S3C shows the disordered averaged correlation length of the carrier density fluctuations, obtained as the full width at half maximum length of the carrier density spatial correlation function. Such correlation length can be interpreted as a measure of the typical size of the electron-hole puddles. Similarly, Fig. S3D shows the dependence on d of the full width at half maximum length of the screened disorder potential spatial correlation function.

Effect of hBN on Global Potential Fluctuations

Fig. S5A shows a hybrid device that includes single-layer and double-layer graphene on SiO_2 , GSiO_2 , and GGSiO_2 , respectively, as well as single- and double-layer graphene on hBN in close proximity. The white dashed line represents the edges of two stacked monolayer graphene flakes. Fig. S5 B and C show the STS gate maps obtained by sweeping the gate voltage at 10 T for GSiO_2 and GGSiO_2 , respectively. Each vertical line represents an LL spectrum at a particular V_g . White staircase pattern corresponds to the LL peaks with level-index N .

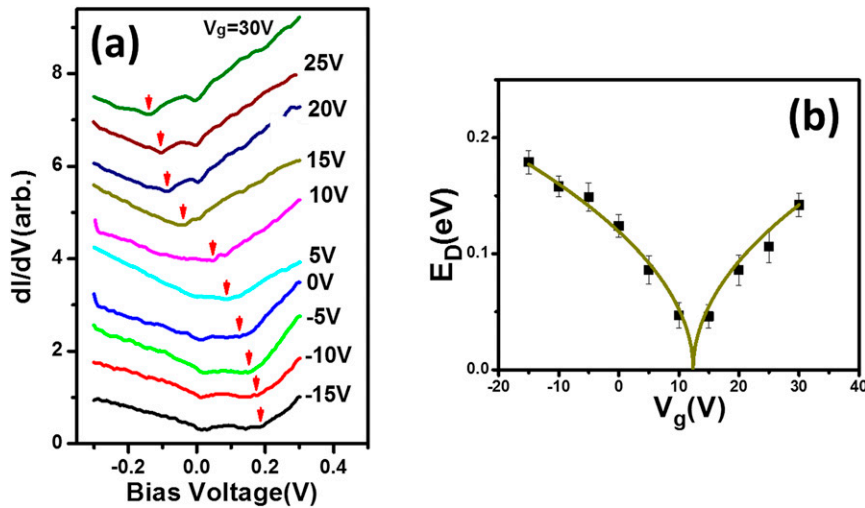


Fig. S1. (A) Gate voltage dependence of dI/dV spectra on GSiO_2 sample. Curves are vertically displaced for clarity. (B) Gate voltage dependence of E_D (squares) together with the fit (solid line) discussed in the text. Tunneling parameters: $I_{set} = 20$ pA, $V_b = 0.3$ V, and modulation voltage 5 mV.

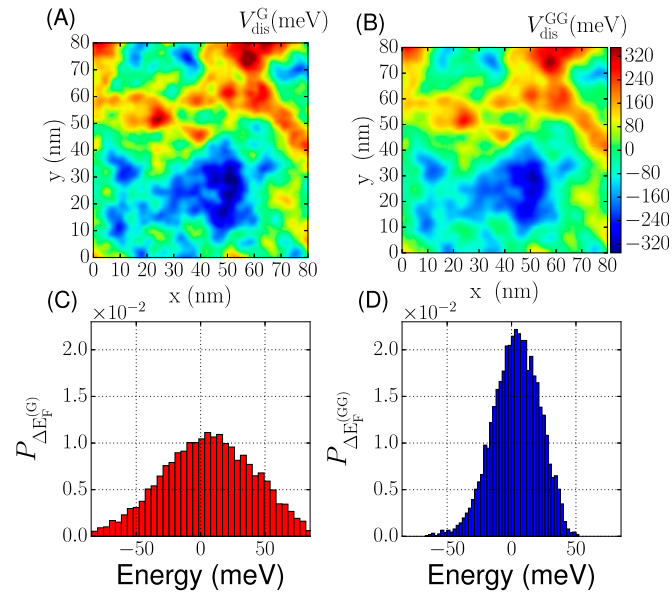


Fig. S2. (A and B) The profiles of the bare disorder potentials, $V_D^{(1)}$ and $V_D^{(2)}$, given by Eqs. S2 and S3, respectively, for the same parameter values and disorder realization used to obtain the profiles for $\Delta E_F \equiv \Delta E_D$ shown in Fig. 2 E and F. We notice that the profiles in A and B are anticorrelated with the profiles of Fig. 2 E and F: red (positive potential) regions in A and B correspond to blue (p-doped) regions in Fig. 2 E and F, and vice versa. This is simply due to the fact that negative (positive) charge impurities induce a local decrease (increase) of the electron density. By comparing the scale of the color plots in B and Fig. 2F we can notice the dramatic reduction of the strength of the disorder potential in GGSiO₂. (C and D) Histograms of local potential fluctuations for G and GG, respectively, obtained after disorder averaging over 600 disorder realization for the same impurity density and doping realization used to obtain A and B from Fig. 2 E and F: $n_{\text{imp}} = 5 \times 10^{11} \text{ cm}^{-2}$; carrier density $n = 10^{12} \text{ cm}^{-2}$.

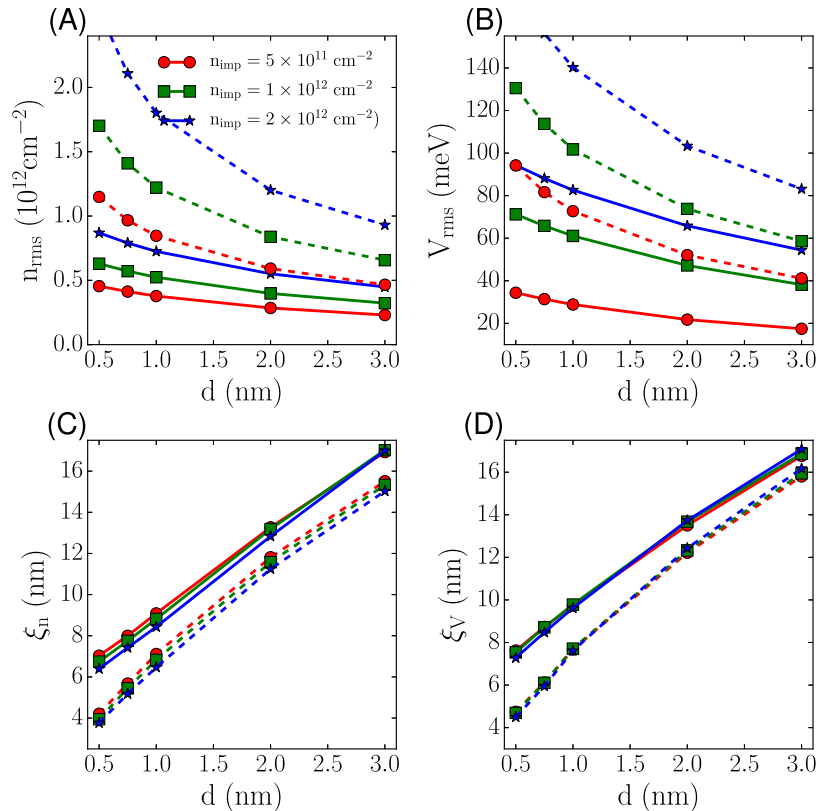


Fig. S3. Scaling of the amplitude of the carrier density fluctuations (A), screened disorder (B), puddle correlation length (C), and screened disorder correlation length (D), as a function of the average distance d between charge impurities and the double layer graphene, for different values of the impurity density. The dashed lines show the results for GSiO₂ and the solid lines the ones for GGSiO₂. Here the distance between the two graphene layers is set equal to 0.7 nm (as in the other theoretical results) and the doping $n = 10^{11} \text{ cm}^{-2}$.

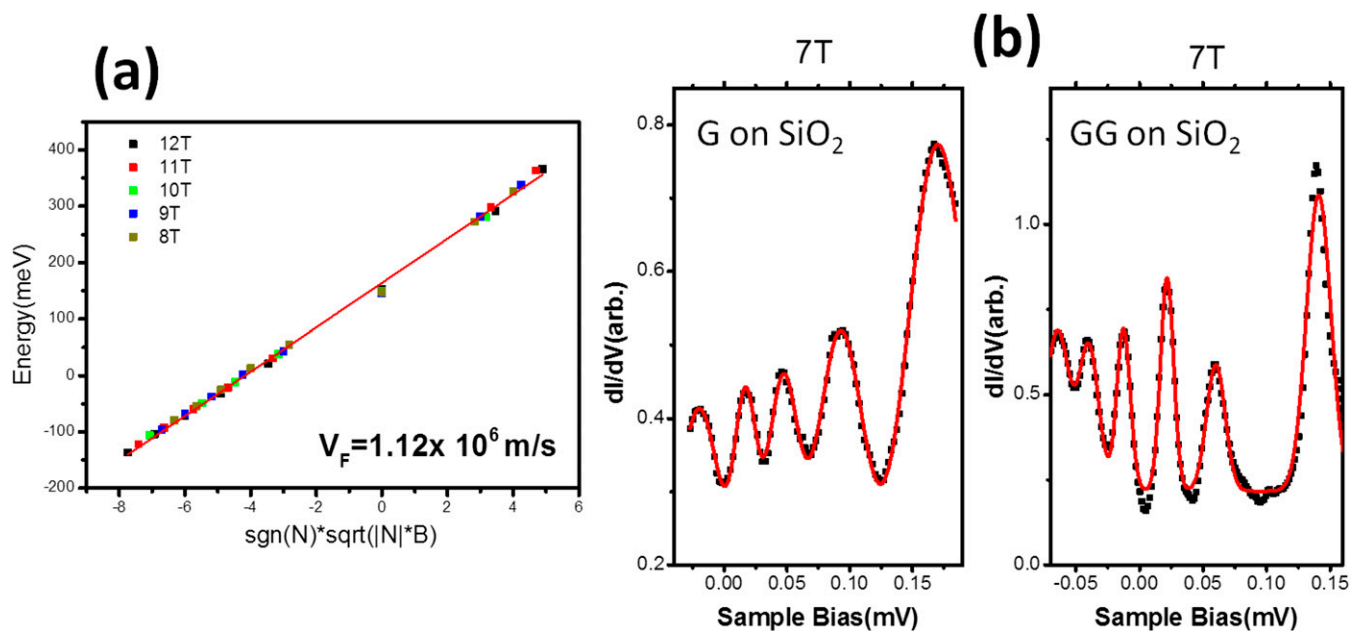


Fig. 54. (A) LL energies (solid symbols) for fields in the range $B = 8$ T to 12 T are plotted against the reduced parameter $\text{sgn}(N) \cdot \sqrt{|N|B}$ for the GGSiO₂ sample. The solid line is a linear fit to equation $E_N = E_D \pm v_F \sqrt{2e\hbar|N|B}$ $n = 0, \pm 1, \pm 2, \pm 3, \dots$, yielding a characteristic Fermi velocity of $v_F = (1.12 \pm 0.01) \times 10^6$ m/s. (B) LL spectra (symbols) measured at 7 T in the GSiO₂ (Left) and GGSiO₂ (Right) samples, together with a Gaussian fit (solid lines). Using a constant linewidth to fit the entire spectrum we obtain linewidths of 42 mV and 18 mV for the GSiO₂ and GGSiO₂ samples, respectively.

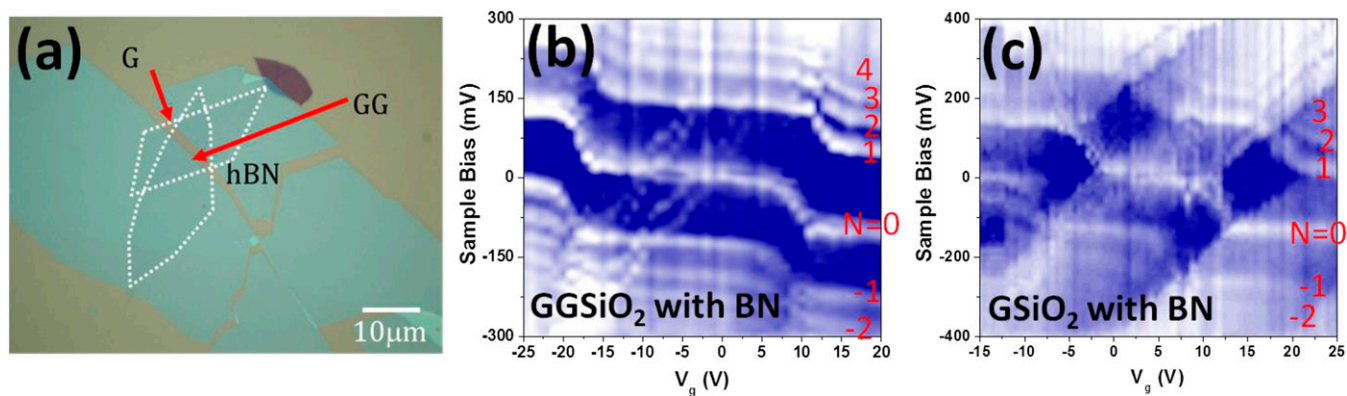


Fig. 55. (A) Optical micrograph of a typical sample showing single (G) and double (GG) graphene layers in the proximity of hBN. (B and C) Gate voltage maps of LLs at 10 T for GSiO₂ and GGSiO₂. The substrate is SiO₂ but in both cases the sample is close to an hBN flake. Tunneling parameters: $I_{\text{set}} = 20$ pA, $V_{\text{ac}} = 5$ mV, $V_b = 0.3$ in A, and $V_b = 0.4$ in B.